Interaction of Laser Pulses with the Water Surface – Theoretical Aspects and Experimental Results

Interaktion von Laserpulsen mit der Wasseroberfläche – Theorie und Praxis

Gottfried Mandlburger

Exact water level heights are required in laser bathymetry as the basis for measuring correct water depths, in hydraulic modelling as reference data for calibrating flood maps, for discharge estimation in hydrology, for topographic map production, and in many other fields. Measuring water surface heights with lasers is feasible but the interaction of the laser beam with the air-water-interface is complex. In this contribution, first, the various parameters influencing the backscatter from the water surface and water column (laser wavelength, incidence angle, beam divergence, footprint size, surface albedo, specular reflection, etc.) are discussed in theory based on the laser-radar equation. In the second part, results from various real-world data acquisitions with topographic and bathymetric laser sensors are presented demonstrating the effect of the individual parameters in practice.

Keywords: Water surface mapping, airborne laser bathymetry, laser-radar equation, scattering and absorption, water surface dynamics

Präzise Wasserstandshöhen werden in verschiedenen Anwendungsgebieten benötigt: In der Laserbathymetrie für die Ermittlung korrekter Wassertiefen, in der hydrodynamisch-numerischen Modellierung als Referenzdaten für die Kalibrierung von Modellen zur Ableitung von Überschwemmungsflächen, in der Hydrologie für die Durchflussbestimmung, in der Kartographie für die Erstellung topographischer Karten und in vielen anderen Bereichen. Die Erfassung der Wasseroberfläche mittels Laserentfernungsmessung ist zwar prinzipiell möglich, allerdings ist die Interaktion der Laserstrahlung mit der Wasser-Luft-Grenzschicht komplex. In diesem Beitrag werden daher zunächst die wesentlichen Parameter, die bei der Rückstreuung des Signals von der Wasseroberfläche und der Wassersäule eine Rolle spielen, anhand der Laser-Radar-Gleichung theoretisch erörtert (Laserwellenlänge, Einfallswinkel, Strahldivergenz, Größe des Abtastflecks, Albedoeffekt, spiegelnde Reflexion usw.). Im zweiten Teil werden Ergebnisse von konkreten Messkampagnen mit topographischen und topo-bathymetrischen Laserscannern vorgestellt, die den Einfluss der einzelnen Parameter in der Praxis zeigen.

Keywords: Wasseroberflächenbestimmung, Laserbathymetrie, Laser-Radar-Gleichung, Strahlablenkung und Absorption, dynamische Wasseroberflächen

1 INTRODUCTION

Knowledge of exact water level heights and water body extents is crucial in many fields including geodesy, ecology, hydrobiology, hydraulic engineering, and economy. Flood extents, for example, have a high socio-economic but also ecological impact /European Union 2000/, /European Union 2007/. Flood simulations are therefore crucial not only for insurance companies but also for hydraulic engineers to ensure the structural safety of flood protection measures, for fluvial morphologists as floods are the main drivers for fluvial change, and for biologists as periodic inundation of alluvial forests is essential for the integrity of aquatic and terrestrial habitats /European Union 1992/.

Synthetic Aperture Radar (SAR) from satellite platforms and aerial stereo-photogrammetry are the established methods for large-scale mapping of water body boundaries /Musa et al. 2015/, /Marcus & Fonstad 2008/. These techniques make use of the distinct appearance of water and land in the captured data. This applies to both passive images measuring the backscatter of the solar radiation and SAR images recording the backscatter of an active microwave radar source. The main product is the water-land-boundary describing the transition line between submerged areas and dry ground.

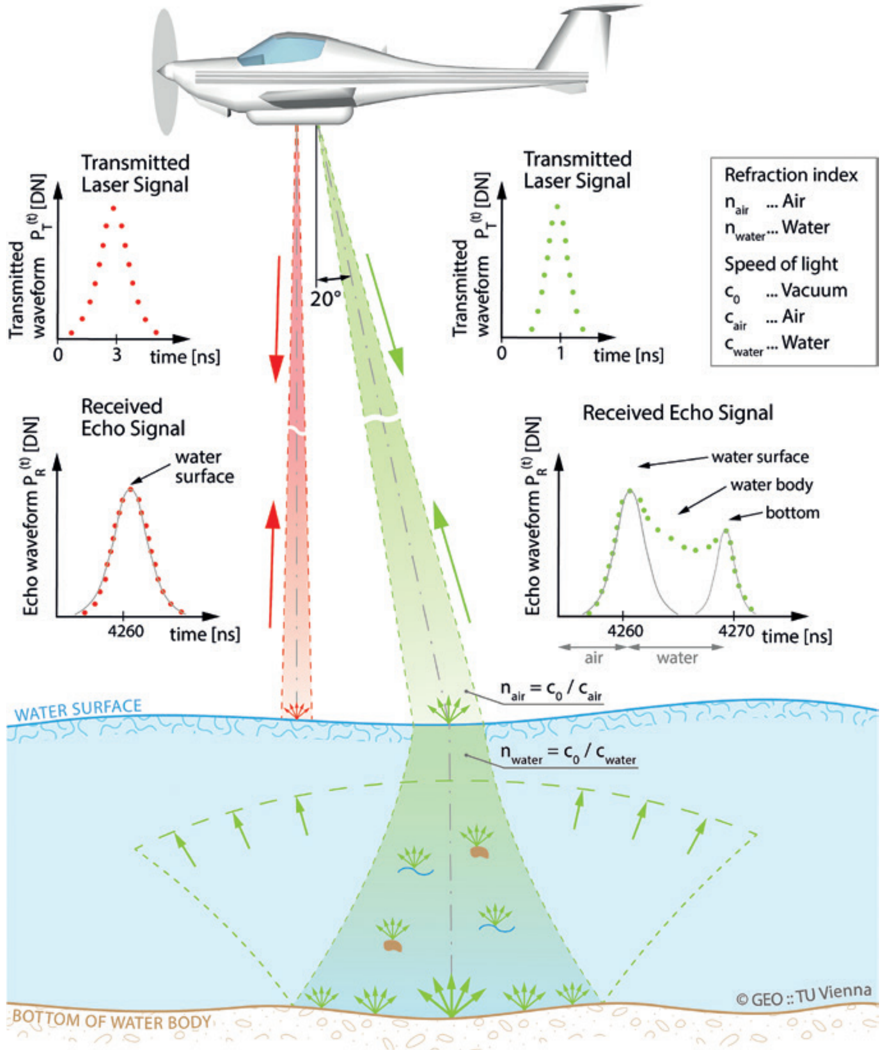

Fig 1 | Interaction of green (λ = 532 nm) and near infrared (NIR, λ > 1 µm) laser signal with the medium water

Areal capturing of water level heights, in contrast, is feasible with laser scanners based on the time-of-flight measurement principle (*cf. Fig. 1*). A train of laser pulses is emitted from the scanner mounted on an airborne platform, travels through the atmosphere, interacts with the water surface, and the receiver detects the reflected part of the backscatter. The distance is proportional to the measured round-trip time. In theory, a 3D point on the water surface can be obtained for every single laser pulse providing the basis for the calculation of a dense digital water surface elevation model. One of the main applications is airborne laser bathymetry (ALB), where a pulsed green laser (λ = 532 nm) is used to capture the bottom topography of the water body /Guenther et al. 2000/. Although the main purpose of ALB is measuring water depths, knowing the exact position of the air-water-interface surface is an inevitable precondition for performing proper range and refraction correction of the laser beam travelling through two media. However, the interaction of the laser signal with the medium water in general and the water surface in particular is complex. It depends on instrumental, environmental, and mission parameters (laser wavelength, laser beam divergence, water turbidity, water surface roughness, incidence angle, etc.).

The objective of this paper is to review the laser-water interaction in theory based on the laser-radar equation (Section 2) and to illustrate the theoretical findings by analyzing the results from various real-world data acquisitions with topographic and topo-bathymetric laser sensors mounted on airborne platforms (Section 3). The main conclusions are summarized in Section 4.

2 THEORY

The laser-radar equation describes the fundamental relationship between the emitted and the received power (e.g. /Pfeifer et al. 2016/).[1]

$$P_R = \frac{P_T}{(\gamma R)^2\,\pi/4} \cdot \sigma \cdot \frac{D^2\,\pi/4}{4\pi R^2} \cdot \eta_{ATM}\,\eta_{SYS} + P_{BK}. \qquad (1)$$

[1] A list of all symbols used in the formulae is provided on the page 351.

The received power P_R depends on the transmitted power P_T, the measurement range R, the laser beam divergence γ, the size of the receiver aperture D, the laser cross-section σ describing all properties of the target, as well as factors related to system losses η_{ATM} and atmospheric attenuation η_{SYS}. P_{BK}, finally, indicates solar background radiation that degenerates the signal-to-noise ratio.

The laser-radar cross-section σ can be separated into the illuminated target area A, the reflectance ρ of the illuminated object, and the solid angle Ω:

$$\sigma = \frac{4\pi}{\Omega} \cdot \rho \cdot A. \tag{2}$$

Ω, hereby, denotes the opening angle of a cone into which the laser signal is backscattered (cf. *Fig 2*). Specular reflection is characterized by a narrow cone (i.e. small values of Ω). Most of the natural targets like soil, grass, asphalt, trees, etc. are diffuse scatterers. For ideal diffusely reflecting targets ($\Omega = 180°$) Lambert's cosine law is applicable.

The cross-section further depends on the illuminated area A, which is a function of the measurement range R, the beam opening angle γ, and the incidence angle α between the laser beam and the normal direction of the illuminated surface. For targets larger than the laser footprint, the area calculates to /Roncat et al. 2012/:

$$A = \frac{A_L}{\cos\alpha} \approx \frac{(\gamma R)^2 \pi}{4 \cos\alpha}. \tag{3}$$

A_L is the projection of the effectively illuminated target area to a plane orthogonal to the laser beam direction which only depends on the measurement range R and the laser beam opening angle γ. Inserting Eqs. (*3*) and (*2*) into Eq. (*1*) reveals a decrease of received power with the squared sensor-to-target distance (R^2). Linear targets (e.g. power line) crossing the laser footprint, in turn, result in a R^3 relationship and the signal loss corresponds to R^4 for point features (e.g. leafs).

For laser beams hitting water, we choose a specific formulation of Eq. (*1*) that separates the signal contributions from the water surface (P_{WS}), the water column (P_{WC}) and the bottom of the water body (P_{WB}) /Abdallah et al. 2012/, /Tulldahl & Steinvall 2004/:

$$P_R = P_{WS} + P_{WC} + P_{WB} + P_{BK}, \tag{4}$$

$$P_{WS} = \frac{P_T D^2 \pi/4 \, \eta_{ATM} \, \eta_{SYS} \, L_0 \cos\alpha_A}{\pi H^2}, \tag{5}$$

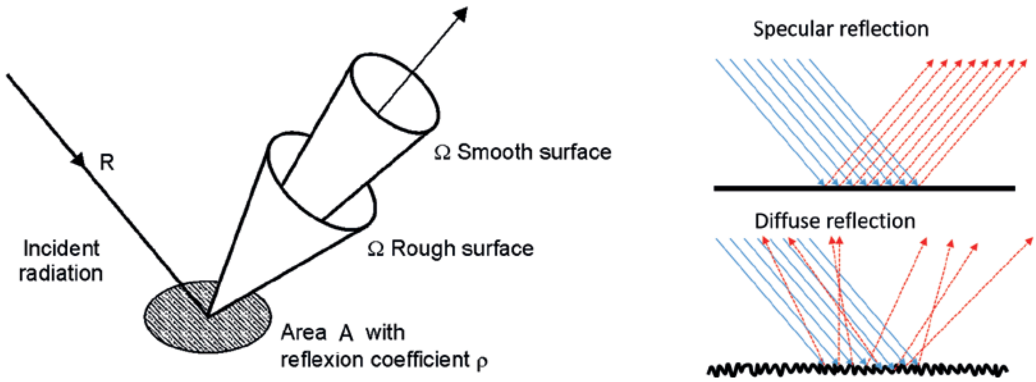

Fig 2 | Specular and diffuse reflection at opaque targets

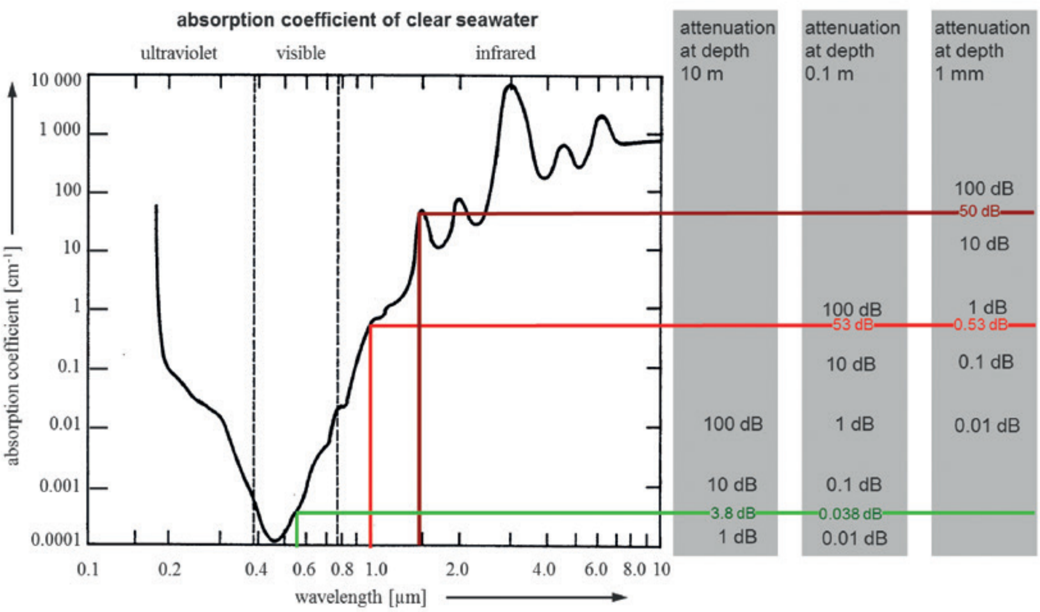

Fig 3 | Wavelength dependent absorption coefficient of clear seawater /Pfennigbauer & Ullrich 2011/

$$P_{WC}(z) = \frac{P_T\, D^2\, \pi/4\, \eta_{ATM}\, \eta_{SYS}\, F(1-L_0)^2 \beta(\varphi)\, e^{\frac{-2kz}{\cos \alpha_w}}}{\left(\frac{n_W H + z}{\cos \alpha_A}\right)^2}, \tag{6}$$

$$P_{WB} = \frac{P_T\, D^2\, \pi/4\, \eta_{ATM}\, \eta_{SYS}\, F(1-L_0)^2 R_B\, e^{\frac{-2kZ}{\cos \alpha_w}}}{\pi \left(\frac{n_W H + z}{\cos \alpha_A}\right)^2}. \tag{7}$$

The signal attenuation within the water column results from scattering at small particles and signal absorption, and is described by the diffuse attenuation coefficient k denoting the degradation rate of light with depth. k consists of a downwelling and an upwelling component /Lyzenga et al. 2006/. Whereas the prior causes beam broadening and loss of spatial resolution, the latter limits the accuracy when determining the water surface level. Eqs. (*6*) and (*7*) describe the contribution of the water column and the bottom of the water body. In both formulae, the exponential term describes the decrease of the received power depending on the water depth (Z), the diffuse attenuation coefficient k, and the local incidence angle of the laser beam in water α_w. This results in the typical, asymmetric echo waveform shown in *Fig. 1*. The k-coefficient consists of two parts: (i) wavelength dependent signal absorption and (ii) scattering depending on the optical properties of water (i.e. turbidity). *Fig. 3* /Pfennigbauer & Ullrich 2011/ shows the strong wavelength dependency of the absorption coefficient for clear sea water. The typical NIR lasers used for topographic mapping operating at wavelengths of 1 064 nm or 1 550 nm, respectively, exhibit high signal absorption. Water is practically impenetrable for these wavelengths (signal loss per 1 mm = 53 dB at a wavelength λ = 1550 nm). Absorption is least for $\lambda \approx$ 480 nm (blue), however, the commonly used wavelength in airborne laser bathymetry is λ = 532 nm derived by frequency doubling of a 1 064 nm Nd:YAG laser. At this wavelength, the absorption is still only 3.8 dB per 10 m water column, thus, allowing capturing water depths of 15–50 m depending on the sensor system (P_T, γ, D, η_{SYS}) and the bottom reflectivity (in Eq. (*7*)).

Our main interest in the context of this paper, however, is the interaction of the laser signal with the water surface. The contribution of the interface return (P_{WS}), is detailed in Eq. (*5*). Besides the already discussed parameters (D, η_{ATM}, η_{SYS}), the measurement range R is hereby expressed via the flying height H and the air-sided incidence angle α_A. L_0 is a factor describing the loss of transmission through the surface (i.e. surface albedo). Using the geometric model of /Cook & Torrance 1982/, L_0 is calculated by the bidirectional reflectance distribution function (BRDF) of the water surface represented by micro-facets.

$$L_0 = \frac{k_d}{\pi} + \frac{k_s\, D_{BS}\, O\, F_r}{\pi \cos^2 \alpha_A}. \tag{8}$$

k_d and k_s denote the diffuse and specular components with $k_d + k_s = 1$, D_{BS} the micro-facet slope distribution function, O the geometric BRDF attenuation factor, and F_r a function describing the Fresnel reflection of light on each micro-facet. The function D_{BS} represents the fraction of the facets that are oriented in the direction of the laser beam. /Beckmann & Spizzochino 1987/ proposed a generic formula that is applicable to a wide range of materials and surface conditions ranging from smooth to very rough.

$$D_{BS} = \frac{1}{r^2 \cos^4 \alpha_A} e^{-(\tan \alpha_A / r)^2}, \tag{9}$$

where r is the root mean square slope of facets (in radians) indicating surface roughness. As the water surface is almost a specular reflector ($k_s \approx 1$), the entire loss of transmission at the water surface is dominated by the slope variation (r) within the laser footprint, in other words by the water surface roughness, and by the air-sided incidence angle of the laser beam (α_A). Small values of r indicate smooth water surfaces resulting in a distribution that is highly directional around the specular component /Cook & Torrace 1982/. For an ideally flat water surface (no waves) the law of reflection (i.e. incoming incidence angle equals incidence angle of reflected ray) applies and, thus, reflections from the water surface are restricted to nadir laser beams, as in all other cases the backscattered light does not reach the sensor. For rough water surfaces ($r > 0$) the likelihood that a portion of the emitted signal is reflected back to the receiver increases although the overall signal strength of the water surface return decreases with increasing r.

To illustrate the latter, *Fig. 4* shows the progression of D_{BS} as a function of r for four representative incidence angles. In topographic laser scanning, the scanning plane is typically vertical with scan angles from –30° to +30° passing the nadir direction (0°). In laser bathymetry, conical scanning is employed (Palmer scanner) with typical cone opening angles between 14° and 20°. Nadir laser beams (blue line) show high D_{BS}-values for smooth water surfaces only (i.e. small values of r) highlighting the high impact of specular reflection when the laser beam hits the smooth water surface under a normal angle. Increasing surface roughness causes a sharp drop of the micro-facet slope distribution function in this case. In all other cases (off-nadir angles: 14°/20°/30°) the D_{BS}-value peak does not

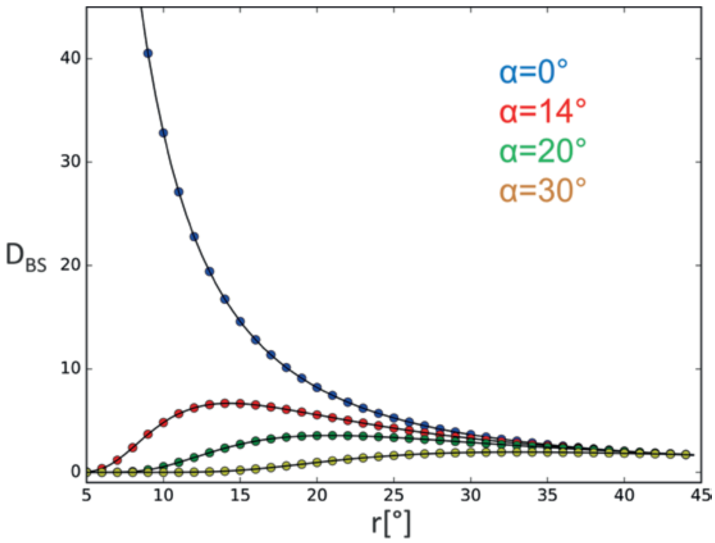

Fig 4 | Micro-facet distribution function D_{BS} depending on water surface roughness r for incidence angles of 0° (blue), 14° (red), 20° (green), and 30° (yellow) occur at smooth water surfaces but rather where r, the root mean square slope of facets, matches the incidence angle α. Please note that for better readability r is plotted in degrees in *Fig. 4* whereas the values are input in radians into Eq. (*9*).

To sum it up, whereas signal attenuation within the water column strongly depends on the laser wavelength and the water clarity, the energy of laser returns reflected from the interface depends on the incidence angle and the water surface roughness. As water mainly acts as a specular reflector, larger beams divergences, resulting in a larger laser footprint diameter at the water interface, increase the chance for obtaining surface echoes.

3 RESULTS

In this section, results from real-world data acquisitions are presented illustrating the theoretical reasoning of the previous section. The study area Neubacher Au (*Fig. 5*) is located at the tailwater of the pre-alpine Pielach River, a right hand tributary of the Danube River in the eastern part of Austria (48° 12' 50" N, 15° 22' 30" E; WGS 84, cf. *Fig. 5b*). The studied, meandering river section is located within a nature conservation area and the adjacent riparian forest is subject to periodic inundation during annual flood events /Mandlburger et al. 2015a/. Gravel mining within the flood plain resulted in a series of ground water ponds that are now used for fishing or recreational purposes. The Pielach River is a riffle-pool-type gravel bed river. Due to the winding course, occasional point bars, varying water depths (ca. 0.5 – 3 m), and varying grain sizes of the bottom substrate (mean diameter: 6.3 cm with occasional larger boulders) the shape and smoothness of the water surface is heterogeneous. High flow velocity combined with shallow water depth (i. e. riffle) results in a rough water surface with typical wave heights of 5 – 10 cm and wave lengths of ca. 2 m /Mandlburger et al. 2015b/. Smooth water surfaces, in contrast, occur at deep pools and shallow backwater areas (cf. *Fig. 5c*). Even smoother, mirror-like water surfaces are observed at standing waters (ponds, cf. light blue polygons in *Fig. 5a*) when captured in still air conditions.

The study area was repeatedly captured with a Riegl VQ-880-G topo-bathymetric laser scanner mounted on a Diamand DA42 light aircraft from a flying altitude of 600 m a.g.l. The scanner emits green laser pulses (λ = 532 nm) with a pulse repetition rate of 550 kHz and the conical scanning mechanism (Palmer scanner) provides a constant off-nadir angle of 20° and a circular scan pattern on the ground. The backscattered echo waveforms are digitized with

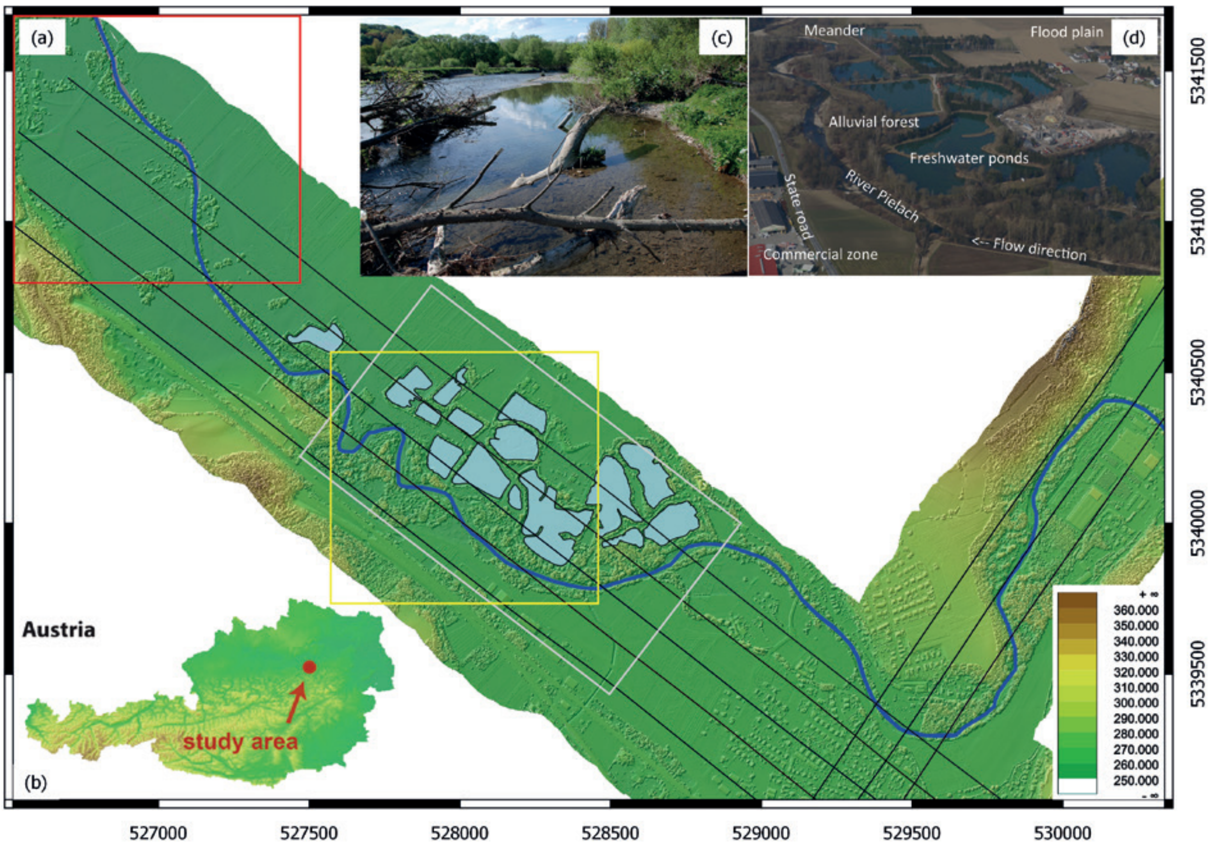

Fig 5 | Study area Neubacher Au, Pielach River; (a) Flight block overview, image background: DEM, shaded relief map superimposed with color coded elevation map, the color legend is plotted in the lower right image corner; dark blue line: axis of Pielach River, light blue polygons: freshwater ponds, black lines: flight trajectories, thick white line/yellow rectangle/red rectangle: details *Fig. 6*, *Fig. 7*, *Fig. 8*; (b) overview map of Austria, location of study area marked with red circle; (c) terrestrial photo showing smooth backwater areas and deadwood in the foreground and the rough main channel in the background; (d) aerial photo taken from the cockpit during data acquisition, the visible area is marked with a grey rectangle in (a)

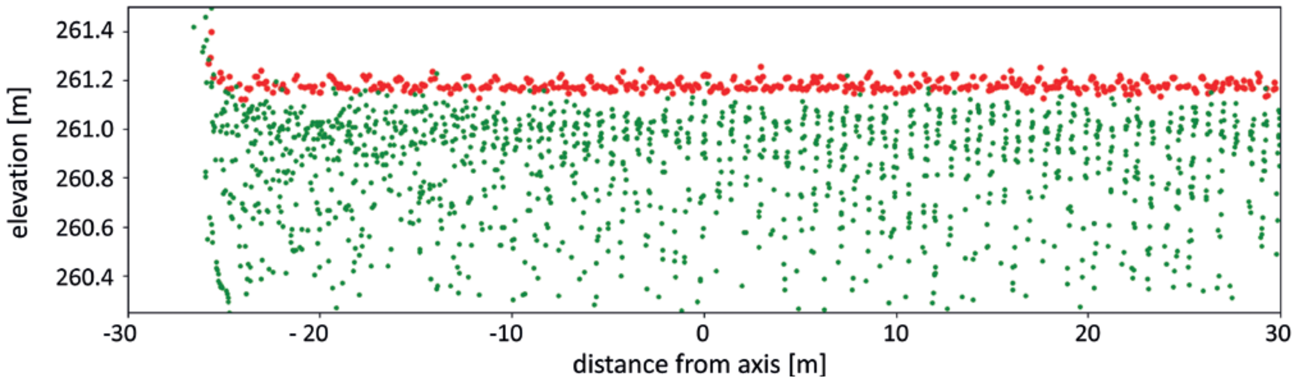

Fig 6 | Cross sectional view depicting different water penetration behavior of NIR and green laser radiation. Section depth: 2 m.

2 GHz frequency and the sensor supports online waveform processing as well as storage of the entire waveform for off-line waveform analysis in post-processing. The data presented in this section were captured on April 14, 2015 (first days of foliation period) and on June 16, 2016 (full leaf-on). For the latter flight, the system was equipped with an optional NIR laser channel ($\lambda = 1\,064$ nm). In contrast to the green channel, the NIR beams are deflected via a polygonal mirror resulting in parallel scan lines orthogonal to the flight trajectory. The off-nadir angles hereby range from –20° to +20°. The green laser beams are deliberately widened to ensure eye safety of the class 3B laser. With a beam divergence $\gamma = 1$ mrad, the resulting laser footprint diameter d on the ground is 60 cm. In contrast to that, the NIR beams are more collimated ($\gamma = 0.2$ mrad, $d = 15$ cm). It should be noted that, as the NIR and the green laser beams are not collinear, the water surface returns from the NIR channel can only then be used to reconstruct the air-water interface if the water surface is sufficiently static. This, however, applies to the study area (standing water bodies and running water with predominately laminar flow characteristics).

In the following, some of the issues raised in Section 2 are illustrated with real data starting with the wavelength-dependent absorption/penetration behavior of the laser signal at the air-water interface. *Fig. 6* shows the cross section marked in *Fig. 5a* (white line). It can clearly be seen that the NIR returns are aligned horizontally with only small deviations due to fluctuations of the (standing) water body and the measurement precision. Almost no penetration into the water column is visible for the NIR returns, which is in line with *Fig. 3* /Pfennigbauer & Ullrich 2011/. The penetration into the water column is limited by a few millimeters for the used near infrared wavelength $\lambda = 1\,064$ nm. It should be noted that the penetration would even be less for $\lambda = 1\,550$ nm, the other commonly used wavelength in topographic laser mapping. The green returns, in contrast, only rarely coincide with the NIR returns but in general penetrate approximately 10–25 cm into the water column. This means that apparent green returns from the water surface in fact are composed of direct reflections from the interface as well as volume backscatter from just beneath the water surface. /Guenther et al 2000/ state that the amount of penetration is difficult to quantify as the ratio between interface and sub-surface signal portions is subject to considerable variation depending on water surface roughness, water clarity, etc. However, some of the water surface returns show good agreement with the nearest NIR returns and only very few green echoes are too high. This opens the floor for estimating the water level using green laser returns only by employing statistical analysis if the spatial neighborhood is large enough. /Mandlburger et al. 2013/ quantified the near surface penetration of the green laser signal using statistical approaches and concluded that the underestimation of the water surface level can be kept below 6 cm depending on the water clarity and the neighborhood size used for spatial aggregation.

According to the laser-radar equation, the signal component from the water surface (*Eqs. 5* and *8*) depends on the incidence angle between the laser beam and the water surface normal direction (α_L). For a section of a flight strip marked with a yellow rectangle in *Fig. 5a*, *Fig. 7* shows the signal amplitude maps of NIR (a) and green (b) laser returns together with the flight trajectory (black line) of the respective strip. As stated above, due to the employed scanning mechanism the incidence angles of the NIR laser beams w.r.t. a horizontal plane range from –20° at the beginning of the scan line via nadir looks in the middle of the scan line to +20° at the scan line end. For diffusely reflecting targets on dry ground, the signal amplitude drop of the NIR returns towards the strip boundary is hardly noticeable in *Fig. 7a*. However, the high degree of specular reflection at the water surface causes a sharp drop of the point density and the signal strength with increasing distance from the center of the scan line, i.e. with increasing off-nadir angles. Beyond an incidence angle of approx. 5–10°, most of the energy is no longer reflected towards the receiver FOV. This effect was further investigated in detail for the NIR water surface returns of two ponds. In *Fig. 7c*, the color coded NIR water surface echo amplitudes show a clear tendency from the center towards the edge of the flight line (increasing incidence angle, decreasing signal amplitude); *Fig. 7d*, finally, shows the scatterplot of both attributes from which the drop of signal amplitude with increasing incidence angle is clearly perceivable. The highest signal amplitudes occur for returns with small incidence angles, but low amplitudes can also be observed for small incidence angles. This is because of small wind induced waves causing a deviation of the actual water surface from perfect planarity. However, for larger incidence angles less water surface returns in general, and lower signal amplitudes in particular are observed.

The signal amplitude distribution of the green channel shown in *Fig. 7b*, in contrast, is homogeneous for each pond with variations

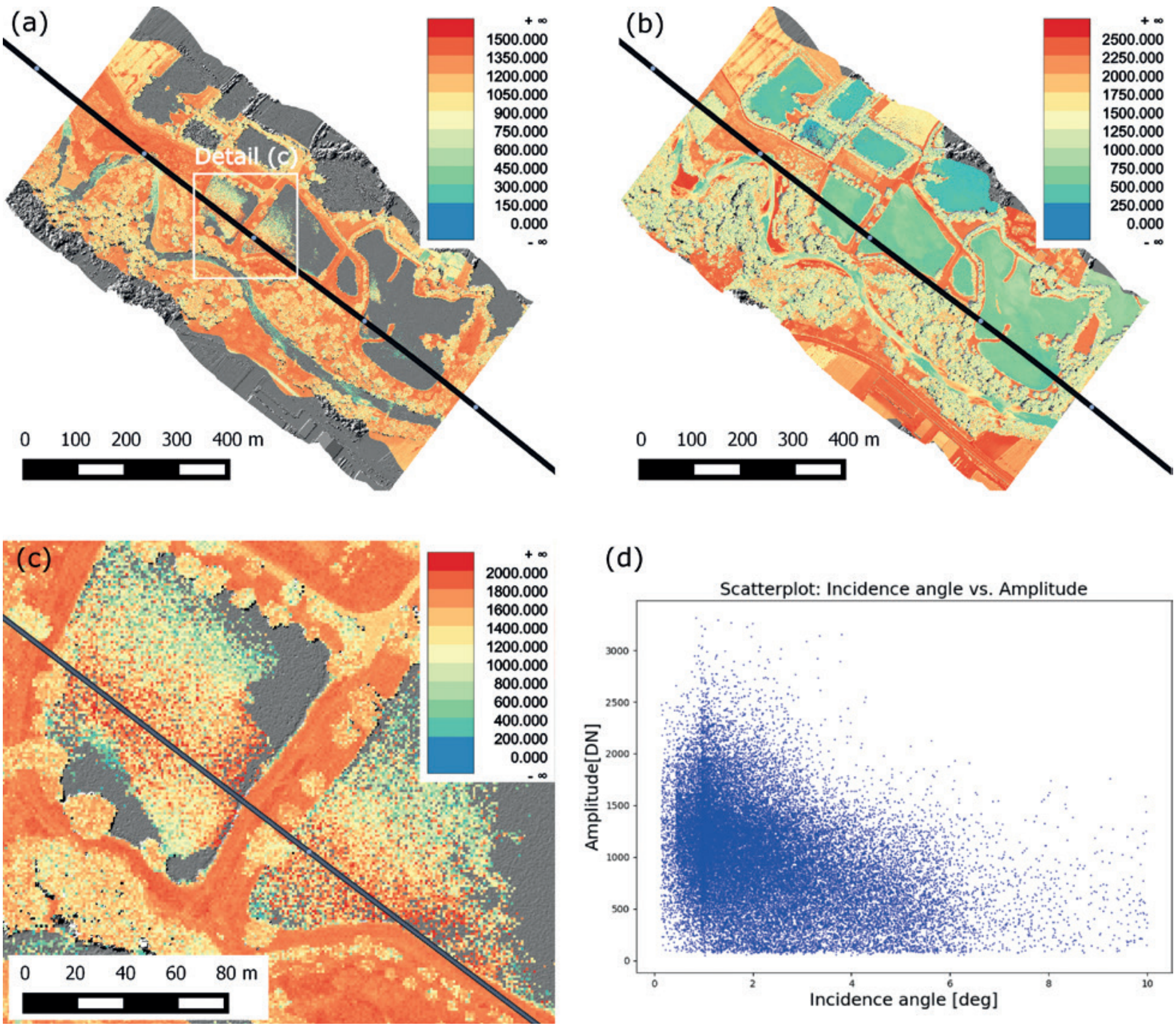

Fig 7 | Color coded map of signal amplitude (peak power [DN]) for NIR (a) and green (b) laser channel; black line: flight trajectory; (c) detail: NIR signal amplitude map of pond water surface area; (d) scatterplot: signal amplitude vs. incidence angle of NIR water surface returns from one pond to the next. The reasons for these different characteristics are:

i. The conical scan pattern ensures a constant off-nadir angle of 20°, which explains the homogeneous point density and signal amplitude. The observed variation of the latter depends on the varying water clarity of the individual ponds.
ii. The larger footprint diameter of the green compared to the NIR laser beams together with the micro roughness of the water surface increases the probability for parts of the reflected energy being backscattered in the direction of the receiver.
iii. The green returns are a mixture of interface and sub-surface reflections. Following the line of argument concerning the incidence angle dependency of the NIR signal above, the portion of pure green interface returns can be considered low for the constant 20° angle. Most of the received energy therefore stems from volume backscattering in the topmost layer of the water column.

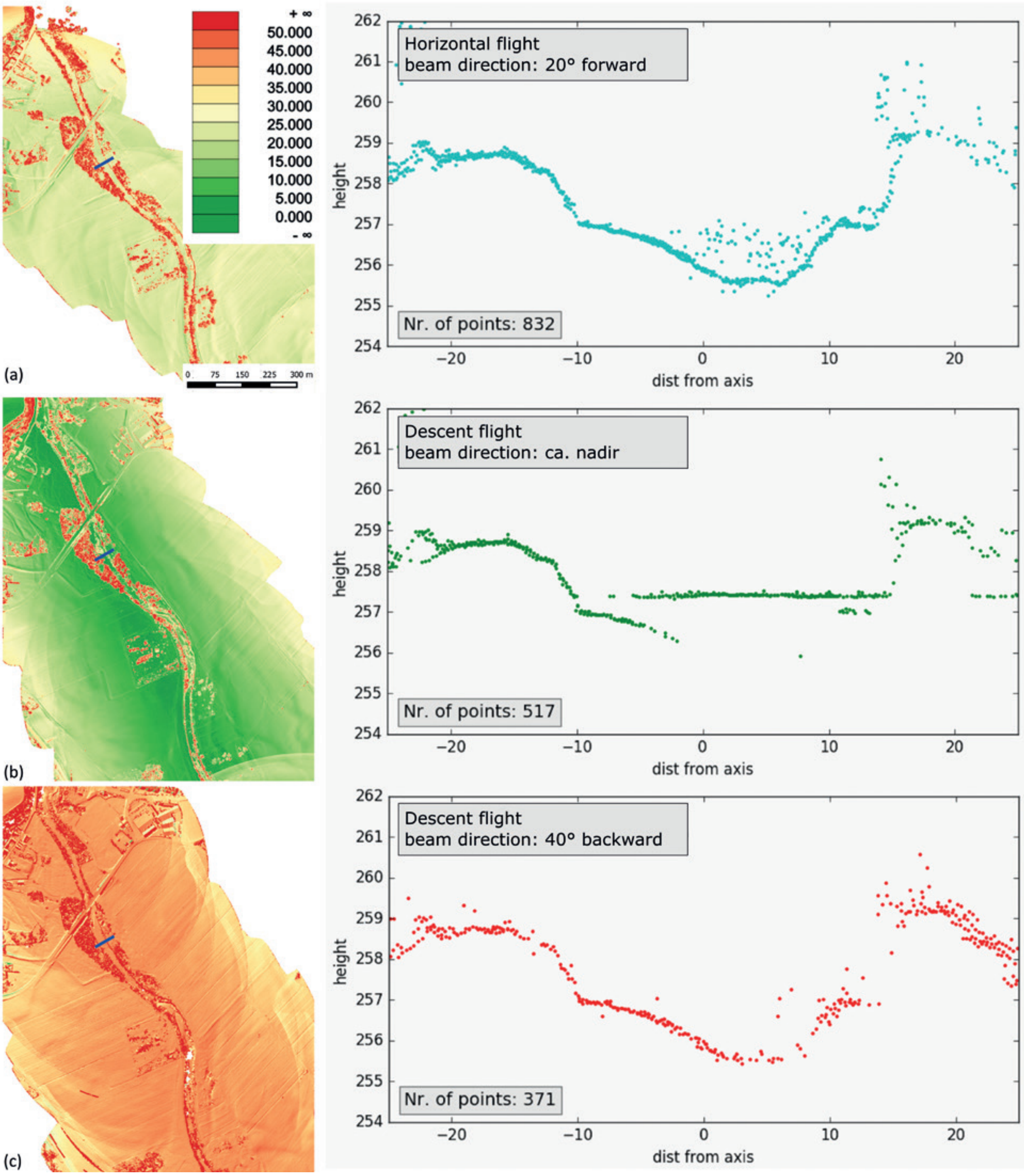

Fig 8 | Descent flight experiment; left: color coded incidence angle maps, angles in degrees, right: corresponding point cloud of a representative river cross section (location: blue line in left image); (a) horizontal flight, incidence angle 20° (b, c) descent flight, forward/backward looking semicircle, incidence angle 0°/40°

P_T	Transmitted laser power in W
P_R	Entire received laser power in W
P_{WS}	Received power returned from the water surface in W
P_{WC}	Received power returned from the water column in W
P_{WB}	Received power returned from the water bottom in W
P_{BK}	Received power caused by background radiation in W
R	Measurement range in m
γ	Laser beam divergence angle in angular units (a. u.)
σ	Laser-radar backscatter cross section in m^2
D	Receiver aperture area in m^2
η_{ATM}	Atmospheric loss factor
η_{SYS}	System loss factor
Ω	Opening angle of backscatter cone in a. u.
ρ	Diffuse target reflectance
A	Target area in m^2
L_0	Surface albedo factor describing the loss due to transmission through the surface (surface albedo)
α_A	Air-sided incidence angle between laser beam and water surface normal direction in a. u.
α_W	Water-sided (i. e. refracted) incidence angle in a. u.
F	Loss factor (telescope FOV) due to the field of view of the telescope
$\beta_{(\varphi)}$	Volume scattering function
k	Diffuse attenuation coefficient
n_W	Refractive index of water (ca. 1.33)
H	Flying height above water level in m
z	Height of water column in m
Z	Water depth in m
R_B	Bottom albedo factor (i. e. bottom reflectance)
k_d	Diffuse reflection portion
k_s	Specular reflection portion
D_{BS}	Micro-facet distribution function according to Beckmann and Spizzochino (1987)
O	Geometric attenuation factor of the bi-directional reflectance distribution function
F_r	Function describing the Fresnel reflection of light on each micro-facet
r	Root mean square (r. m. s.) slope of the micro-facets in radians

Tab. | Complete list of symbols used in formulae

The above findings raise an interesting question: Like most of the bathymetric sensors, the employed Riegl VQ-880-G instrument uses a conical scanning mechanism with a constant off-nadir angle, thus, preventing laser shots in nadir direction. While the 15–20° off-nadir angle was long found to be the optimum angle for measuring bathymetry /Guenther et al. 2000, and the cited literature therein/, the question arises if green returns from the water surface are also affected by volume backscattering if measured in nadir direction.

To address this question, the following experiment was carried out. A relatively straight section of the Pielach River (cf. *Fig. 5a*, red rectangle) was first captured with an ordinary horizontal flight line, and additionally with a flight line tilted by 20° (i. e. descent flight). That way, the tip of the forward looking semicircle pointed exactly in nadir direction whereas the water surface was hit under a 40° angle at the corresponding tip of the backward looking semicircle. The results are plotted in *Fig. 8*.

Fig. 8 shows on the left side a color coded incidence angle map. For the horizontal flight (*Fig. 8a*) the incidence angle distribution is homogeneous around the nominal value of 20° with only small deviations due to (i) terrain slope variations and (ii) small flight irregularities. Larger incidence angles only occur in vegetated areas. The point cloud of a representative profile of this standard ALB data acquisition variant is shown on the right side in a cross sectional view. The water surface does not appear as a clear boundary line but is rather fuzzy with points from near the water surface directly adjacent to points clearly stemming from the water column. The bottom points, in turn, are dense, consistent and homogeneously distributed over the entire profile. The forward look of the descent flight (*Fig. 8b*) shows a general incidence angle decrease from the river axis (0°) to the strip boundary (25°). As the flight trajectory follows the river course, the laser beams hit the water surface under a normal angle. In the resulting cross sectional point cloud (*Fig. 8b*, right) the water surface returns appear as clear as this is the case for the NIR reflections shown in *Fig. 6* (taken from a different flight of the same area). This supports the assumption that strong direct reflections from the air-water interface are not restricted to infrared wavelengths but also occur using green lasers. The reflection from the interface appears much stronger than the sub-surface volume backscatter. It is furthermore interesting that most of the signal is in fact reflected from the interface and only a smaller portion reaches the water bottom. The respective bottom points are much sparser compared to *Fig. 8a* and the achievable measuring depth is poor. The least favourable variant, though, is the 40° incidence angle from the backward looking semicircle of the descent flight line. Here, neither the water surface nor the river bottom are captured adequately.

4 CONCLUSIONS

In this contribution the interaction of laser light with the medium water in general and the water surface in particular was reviewed. Whereas the general laser-radar equation establishes the fundamental relation between the emitted and the received laser energy, a specific version splitting the signal contributions from the water surface, the water column and the water bottom was used and the most influential parameters therein were analyzed in detail. For targets on dry ground, the measurement range, the laser beam divergence, the size of the receiver aperture and the targets properties are crucial. The latter are summarized in the so-called laser-radar cross section which is influenced by the targets' reflectance and the directionality of the reflected light (both depending on the material), as well as the size of the illuminated target area.

In addition to that, for laser beams hitting water the loss of transmission through the surface (i.e. surface albedo), the water clarity described by the diffuse attenuation coefficient and, again, the reflectance of the water bottom play a role. Among the many parameters influencing the surface albedo, the incidence angle of the laser beam w.r.t the water surface normal direction and the water surface roughness are most important. At smooth water surfaces like, e.g. standing inland water bodies, specular reflection is dominating which results in very high signal peaks in nadir direction and a rapid decrease of the received signal strength with increasing off-nadir angles. The directional sensitivity is less pronounced for rough water surfaces (e.g. waves, riffles) especially if the laser footprint covers multiple wave cycles. In this case, a part of the illuminated surface area is directly facing to the sensor whereas others are averted.

The ability of laser light for penetrating the water column strongly depends on the wavelength. Whereas water is practically impenetrable for the typical NIR wavelengths used for topographic mapping, light in the blue or green domain of the electro-magnetic spectrum shows the least absorption in water. Thus, green lasers are commonly used for measuring shallow water bathymetry. For scanners employing a conical scanning mechanism with constant off-nadir angle of the laser beam, most of the water surface returns lie below the actual water level as interface reflections are mixed with volume backscatter from just below the water surface. Therefore, the water level height is often underestimated when derived from the reflections of the green channel only. NIR laser returns can advantageously be used for areal water surface reconstruction. But such water surface models can only then be used as basis for range and refraction correction of raw green laser beams if the water surface is sufficiently static (ponds, laminar flow).

ACKNOWLEDGEMENTS

The research leading to this manuscript was funded by the German Research Foundation (DFG) project 'Bathymetry by fusion of airborne laser scanning and multi-spectral aerial imagery' and by the Austrian Research Promotion (FFG) project "Alpine Airborne Hydromapping – from research to practice" (AAHM-R2P). The author expresses his gratitude to Dr. Martin Pfennigbauer (Riegl LMS) for providing the data and for valuable discussions on subject matters.

REFERENCES

Abdallah, H.; Baghdadi, N.; Bailly, J.-S.; Pastol, Y.; Fabre, F. (2012): Wa-LiD: a new lidar simulator for waters. In: IEEE Geoscience and Remote Sensing Letters, 9(2012)4, 744–748.

Beckmann, P.; Spizzochino, A. (1987): The scattering of electromagnetic waves from rough surfaces. Artech House, Norwood, MA, USA.

Cook, R. L.; Torrance, K. E. (1982): A reflectance model for computer graphics. In: ACM Transactions on Graphics, 1(1982)1, 7–24.

European Union (1992): Council Directive 92/43/EEC on the Conservation of Natural Habitats and of Wild Fauna and Flora. Brüssel.

European Union (2000): Directive 2000/60/EC of the European Parliament and of the Council of 23 October 2000 Establishing a Framework for Community Action the Field of Water Policy. Brüssel.

European Union (2007): Directive 2007/60/EC of the European Parliament and European Council of October 2007 on the Assessment and Management of Flood Risks. Brüssel.

Guenther, G. C.; Cunningham, A. G.; Laroque, P. E.; Reid, D. J. (2000): Meeting the accuracy challenge in airborne Lidar bathymetry. In: Proceedings of the 20th EARSeL Symposium: Workshop on Lidar Remote Sensing of Land and Sea, Dresden.

Lyzenga, D.; Malinas, N.; Tanis, F. (2006): Multispectral bathymetry using a simple physically based algorithm. In: IEEE Transactions on Geoscience and Remote Sensing, 44(2006)8, 2251–2259.

Mandlburger, G.; Pfennigbauer, M.; Pfeifer, N. (2013): Analyzing near water surface penetration in laser bathymetry – A case study at the River Pielach. In: Proceedings of ISPRS Annals of the Photogrammetry, Remote Sensing and Spatial Information Sciences, Antalya, Turkey, 175–180.

Mandlburger, G.; Hauer, C.; Wieser, M.; Pfeifer, N. (2015a): Topo-Bathymetric LiDAR for Monitoring River Morphodynamics and Instream Habitats – A Case Study at the Pielach River. In: Remote Sensing, (2015)7, 6160–6195.

Mandlburger, G.; Pfennigbauer, M.; Riegl, U.; Haring, A.; Wieser, M.; Glira, P.; Winiwarter, L. (2015b): Complementing airborne laser bathymetry with UAV-based lidar for capturing alluvial landscapes. In: SPIE Remote Sensing 2015, Toulouse, France, Vol. 9637.

Marcus, W. A.; Fonstad, M. A. (2008): Optical remote mapping of rivers at sub-meter resolutions and watershed extents. In: Earth Surface Processes and Landforms, 33(2008), 4–24.

Musa, Z. N.; Popescu, I.; Mynett, A. (2015): A review of applications of satellite SAR, optical altimetry and DEM data for surface water modelling, mapping and parameter estimation. In: Hydrology and Earth System Sciences, 19(2015), 3755–3769. DOI: 10.5194/hess-19-3755-2015.

Pfeifer, N.; Mandlburger, G.; Glira, P. (2016): Laserscanning. In: Freeden, W.; Rummel, R. (Hrsg.): Handbuch der Geodäsie, Band Photogrammetrie und Fernerkundung. Springer, Berlin/Heidelberg, 1–51.

Pfennigbauer, M.; Ullrich, A. (2011): Multi-wavelength airborne laser scanning. In: Proceedings of the International Lidar Mapping Forum, ILMF, New Orleans.

Roncat, A.; Pfeifer, N.; Briese, C (2012): A linear approach for radiometric calibration of full-waveform Lidar data. In: Proceedings SPIE 8537, Image and Signal Processing for Remote Sensing XVIII. DOI: 10.1117/12.970305.

Tulldahl, H. M.; Steinvall, K. O. (2004): Simulation of sea surface wave influence on small target detection with airborne laser depth sounding. In: Applied Optics, 42(2004)12, 2462–2483.

Dr. techn. Gottfried Mandlburger

UNIVERSITY OF STUTTGART
INSTITUTE FOR PHOTOGRAMMETRY

Geschwister-Scholl-Str. 24D | 70174 Stuttgart
gottfried.mandlburger@ifp.uni-stuttgart.de

TU WIEN
DEPARTMENT OF GEODESY AND GEOINFORMATION

Gußhausstraße 27-29/E120 | 1040 Vienna
gottfried.mandlburger@geo.tuwien.ac.at

Manuskript eingereicht: 05.07.2017 | Im Peer-Review-Verfahren begutachtet